International Journal of Machine Tools and Manufacture 135 (2018) 53–64

Contents lists available at ScienceDirect

International Journal of Machine Tools and Manufacture

journal homepage: www.elsevier.com/locate/ijmactool

Hardness, grainsize and porosity formation prediction on the Laser Metal Deposition of AISI 304 stainless steel

Jon Iñaki Arrizubieta[a,*], Aitzol Lamikiz[a], Magdalena Cortina[a], Eneko Ukar[a], Amaia Alberdi[b]

[a] Department of Mechanical Engineering, University of the Basque Country UPV/EHU, Plaza Torres Quevedo 1, 48013, Bilbao, Spain
[b] Tecnalia, Industry and Transport Division, Parque tecnológico de Bizkaia E-202, 48170, Zamudio, Spain

ARTICLE INFO

Keywords:
Laser Metal Deposition
Simulation
Pore formation
Grainsize
Hardness

ABSTRACT

The presented numerical model solves the heat and mass transfer equations in the Laser Metal Deposition process and based on the evolution of the thermal field predicts the grainsize, the resulting hardness and evaluates the pores formation probability in an AISI 304 stainless steel. For this purpose, in a first step, the model calculates the shape of the deposited material and the variations of the temperature field. In a second step, and based on the evolution of the thermal field, the model calculates the resulting hardness of the deposited material, the grainsize and the porosity formation probability after the deposition process. Numerical results are experimentally validated, and good agreement is obtained. Consequently, besides predicting the geometry of the resulting part and the evolution of the thermal field, the developed model enables to evaluate the quality of the deposited material. Therefore, the optimum process conditions and strategy when depositing AISI 304 stainless steel can be determined without initial trial-and-error tests.

1. Introduction

Laser Metal Deposition (LMD) is an additive manufacturing process that is being applied for building whole parts as well as the generation of coatings on existing geometries or even the repair of damaged parts. Herzog et al. analyzed the LMD process and verified that it enables to enhance the surface properties of the base material [1]. Since the LMD process is based on a LASER source, it is possible to add material over a substrate with minimal heat affected zone and geometrical distortions. According to the conclusions reached by Toyserkani et al., LMD enables to obtain a high-quality metallurgical bonding between filler and base materials [2]. Moreover, LMD offers higher accuracy of the final geometries in comparison with arc-based deposition processes. Consequently, LMD is gaining a wide acceptance among the different industrial sectors [3].

However, the quality of the deposited material can be very sensitive to the process parameters and it is common to find internal defects in the deposited material and components can even become scrap due to incorrect process parameters. Besides, variations on temperature gradients and the geometry of the melt pool have detrimental effects on LMD manufactured parts [4]. The determination of the process parameters is usually based on previous trial-and-error experimental tests, which is a tedious and time-consuming procedure. For instance, Peng et al. performed an in-depth study of the influence that the different process parameters have in the LMD processing of nickel alloy samples and the resulting component's quality [5]. Similarly, Shipley et al. presented a significant review of the state of the art of the effect of different process parameters on the microstructure, porosity and residual stress of Selective Laser Melting (SLM) manufactured Ti6Al4V parts [6]. With the aim of finding an alternative solution to the experimental parameter optimization, LMD modeling enables a new way for predicting the geometry and properties of the deposited material. Nevertheless, most of the proposed models only consider a specific number of parameters or introduce a high number of assumptions [7–9], what makes these models less suitable for the industry.

Pinkerton carried out a review of the latest advances in the field of LMD modeling [10]. He concluded that LMD is a very complex process that is usually divided into different sub-processes in order to make it more approachable. The most commonly approached problem when modeling the LMD process is the prediction of the geometry and the resultant thermal field. For instance, Peyre et al. developed an analytical-numerical tool for predicting geometries and thermal fields developed during the LMD process, which was validated for the Ti6Al4V alloy [11]. However, no mechanical properties were evaluated.

Regarding filler material addition, both thermal and mass transportation phenomena must be considered. Pinkerton and Li studied the sensitivity of an LMD system to changes in the distance between the nozzle and the substrate and developed a heat flow model as well as a

* Corresponding author. Department of Mechanical Engineering, University of the Basque Country UPV/EHU, Plaza Torres Quevedo 1, 48013, Bilbao, Spain.
E-mail address: joninaki.arrizubieta@ehu.eus (J.I. Arrizubieta).

https://doi.org/10.1016/j.ijmachtools.2018.08.004
Received 24 January 2018; Received in revised form 8 August 2018; Accepted 13 August 2018
Available online 14 August 2018

model for powder mass deposition rate at different positions [12]. Han et al. developed a model that includes substrate melting, solidification and powder particle heating [13]. Besides, Pinkerton et al. studied the energy and mass balances in the LMD process in order to predict the resulting geometry of the clads. The model was validated with two series of straight single-clad-width walls [14].

Going one step ahead, Alimardani et al. developed a 3D numerical model for predicting the geometrical and thermal properties for a four-clad thickness wall. They concluded that the ratio of trapped powder particles into the melt pool of the first layer is significantly lower than that of the successive layers [15]. The model calculates the shape of the deposited material based on a powder efficiency factor that calculates the percentage of trapped powder inside the melt pool. Peyre et al. [11] presented a similar approach.

The modeling of the geometry of the deposited clad and the prediction of the grain growth after the material deposition are key parameters when components with enhanced mechanical properties are to be manufactured via LMD. In this direction, Vilar et al. presented a study on the deposition of a NiCrAlY alloy. Special attention was paid to the generated microstructure and the quality of the crystals [16]. Promoppatum et al. presented a similar work for the Inconel 718 alloy [17]. They predicted the microstructure of the deposited material based on the estimated thermal history. The convection in the melt pool was not considered in this work because, as authors stated, this simplification has little effect on the melt pool size and temperature gradients. Authors conclude that due to this simplification the model overpredicts the maximum temperature reached at the melt pool by approximately 100 °C, what results in an error below 0.5 μm when modeling the primary dendrite arm spacing. Arrizubieta et al. also evaluated the importance of considering or neglecting the melt pool dynamics when modeling the LMD process and determined a process parameter window where the fluid-dynamic phenomena can be omitted without losing accuracy [18].

In addition, Ocelík et al. studied the relation between the microstructure of single and multiple clads by means of Orientation Imaging Microscopy (OIM) [19]. They concluded that the directional growth of individual grains leads to a dendritic structure and a fiber-like structure, but no numerical tool for transferring the obtained results to other situations was provided.

Another critical parameter in the LMD process is the powder distribution at the nozzle exit. Liu et al. studied the effect of inclining the angle of a coaxial nozzle in the longitudinal section of the deposited track and the corresponding crystal growth [20]. However, the presented mathematical model for predicting the crystal growth was developed only for single clads.

On the other hand, porosity is one of the most typical defects on LMD processed parts and the existence of pores negatively affects the mechanical properties of the final part [21]. Therefore, porosity has become a hot topic within the LMD modeling field. For instance, Bandyopadhyay et al. studied the influence of porosity in Ti6Al4V additively manufactured (AM) parts [22]. They quantified that a 30% porosity reduces the elasticity modulus of the material to the 10% when compared with a fully dense AM part. Therefore, it is important to predict and avoid pore formation. Zhang and Tsai analyzed the porosity formation mechanisms [23]. They concluded that the solidification rate of the melt pool is one of the most relevant factors regarding pore generation. In the same way, Li et al. studied the formation of micropores in SLM deposited AISI 316L parts [24]. Authors conclude that pore generation is reduced by lowering the scanning speed, and therefore, increasing the provided specific energy by the laser [21], [22].

With the aim of providing accurate information about the physical mechanisms that influence porosity evolution during SLM, Xia et al. developed a mesoscale model [25]. They concluded that the evolution of porosity strongly depends on the scanning speed. For instance, a low scanning speed allows the trapped gas bubbles to exit the melt pool, hence reducing porosity. Also, a low scanning speed increases the introduced amount of energy in the substrate, and therefore, minimizes defects such as the inter-layer porosity.

Similarly, Zeng et al. studied the presence of porosity in Ni-based laser deposited coatings [26]. They concluded that the porosity appearance follows a Weibull distribution. However, the model was validated only for single clads and the effect of the overlap was not considered. They also analyzed experimentally the relation between the microstructure and the microhardness profile of the deposited clad, but no model that grounds this statement was presented. Another pore generation mechanism is the lack of fusion or the inter-run porosity, which is due to an insufficient substrate melting and generates lack of adhesion [27].

After analyzing the existing numerical models for LMD, it is noticed that there is no complete simulation model that enables to obtain geometry, hardness, grainsize and porosity of the deposited material. Therefore, in the present research work a 3D model that calculates the resulting geometry and the evolution of the thermal field during the LMD process is developed. Besides, the model enables to evaluate the quality of the deposited material. For this purpose, the model calculates the Dendrite Arm Spacing (DAS), the as-deposited hardness of the material and the porosity formation probability. The model is experimentally validated for an AISI 304 stainless steel with reasonable good agreement between the experimental and estimated values.

2. Numerical simulation of the LMD process

The developed numerical model for the simulation of the LMD process is presented in this section. The model is entirely programmed in *Matlab© R2018a* and it is based on vector and matrix operations, what facilitates the programming and reduces the computational cost. Hereafter, the model basis, the energy/mass transfer, boundary conditions and other relevant points of the model are detailed.

2.1. Computational assumptions

With the aim of reducing the computational cost, some reasonable assumptions have been considered when developing the numerical model:

- Material is supposed to be homogeneous, continuous and isotropic. This assumption is also considered by authors like Pinkerton [14].
- Volume variations as a consequence of temperature variations are negligible.
- The real power of the laser beam that reaches the surface of the substrate (P_{real}) is lower than the programmed value (P_{prog}) due to the laser beam attenuation [28]. Laser beam attenuation due to the plasma, in case it is generated, and the shadowing of the powder particles is considered by the use of a global loss coefficient, named with the letter “A” in Eq. (1).

$$P_{real} = (1 - A)\cdot P_{prog} \tag{1}$$

- Melt pool dynamics are omitted in the LMD model, assumption based on the fast nature of the LMD process and the influence of the injected powder particles [18]. This statement goes in line with the conclusion reached by Wirth et al. after studying the LMD process with a high-speed camera, where they found that, due to the disturbance generated by the impinging powder particles, there is no preferred direction on the melt pool flow [29]. Despite authors like Lei et al. studied the influence of the material movement in the melt pool generated by a laser beam, all those studies were performed without material addition, what drastically changes the behavior of the molten material within the melt pool [30]. Therefore, no movement of the molten material is considered.
- Thermal and physical properties are considered to be constant.

However, in order to increase the accuracy of the model, the conductivity and specific energy of each element are set according to its temperature.

2.2. Model basis

The developed model is based on the differential equation for heat transfer via conduction. The differential equation is solved by the Central-Finite-Difference method, which in the case of the thermal field simulations can be written as an explicit expression and therefore, solved with a low computational cost. The first law of the thermodynamics states that the sum of the generated energy ($dE_{GENERATED}$) and the difference between the energy that enters (dE_{IN}) and leaves (dE_{OUT}) a certain element, equals to the energy accumulation ($dE_{ACCUMULATED}$):

$$dE_{IN} - dE_{OUT} + dE_{GENERATED} = dE_{ACCUMULATED} \tag{2}$$

The difference between the energy that gets in and out of an element in the "X" axis direction can be expressed as it follows:

$$dE_{INx} \rightarrow dq_{dx} = q_{dx}\cdot dy\cdot dz\cdot dt \tag{3}$$

$$dE_{OUTx} \rightarrow dq_{x+dx} = q_{x+dx}\cdot dy\cdot dz\cdot dt \tag{4}$$

$$dE_{INx} - dE_{OUTx} \rightarrow dq_x = (q_x - q_{x+dx})\cdot dy\cdot dz\cdot dt \tag{5}$$

Replacing Eqs. (3) and (4) in Eq. (5) and naming the differential volume of an element as "$dV = dx\cdot dy\cdot dz$", the following Eq. (6) is reached:

$$(dE_{INx} - dE_{OUTx}) = -\frac{\partial q_x}{dx}\cdot dx\cdot dy\cdot dz\cdot dt = -\frac{\partial q_x}{dx}\cdot dV\cdot dt \tag{6}$$

By analogy in the other two dimensions (Y and Z), the difference between the energy input and output in each element is defined in Eq. (7):

$$(dE_{IN} - dE_{OUT}) = -\left(\frac{\partial q_x}{dx} + \frac{\partial q_y}{dy} + \frac{\partial q_z}{dz}\right)\cdot dV\cdot dt \tag{7}$$

The energy transmitted by means of conductivity is defined according to Eq. (8) in the three axes of the modeled volume. As the material is considered isotropic, the conductivity "k" is equal in all directions.

$$q_x = -k\cdot\frac{\partial T}{\partial x};\quad q_y = -k\cdot\frac{\partial T}{\partial y};\quad q_z = -k\cdot\frac{\partial T}{\partial z}; \tag{8}$$

Replacing the conductivity Eq. (8) and considering the Laplacian operator of the thermal field, the Eq. (7) that determines the energy variation of a finite element becomes the following Eq. (9):

$$(dE_{IN} - dE_{OUT}) = -k\cdot\left(\frac{\partial^2 T}{\partial x^2} + \frac{\partial^2 T}{\partial y^2} + \frac{\partial^2 T}{\partial z^2}\right)\cdot dV\cdot dt = -k\cdot\nabla^2 T\cdot dV\cdot dt \tag{9}$$

On the other hand, the energy generated inside an element is defined by means of Eq. (10). The generated energy takes a positive value when the element is a heat source and a negative value when the element is a sink source:

$$dE_{GENERATED} = \pm q_v\cdot dV\cdot dt \tag{10}$$

Lastly, the inner energy variation or the accumulated energy variation is defined by means of Eq. (11), where "ρ" and "c" are the density and specific heat of the material, respectively.

$$dE_{ACCUMULATED} = \rho\cdot c\cdot\frac{\partial T}{\partial t}\cdot dV\cdot dt \tag{11}$$

Replacing Eqs. (9)–(11) in the energy balance Eq. (2), the general equation for conduction that determines the thermal field is obtained:

$$a\cdot\nabla^2 T \pm \frac{q_v}{\rho\cdot c} = \frac{\partial T}{\partial t} \tag{12}$$

In Eq. (12), "c" is the specific heat [kJ·Kg^{-1}·K^{-1}], "q_v" the generated power per volume unit [W·m^{-3}], "ρ" the density of the material [kg·m^{-3}] and "a" the thermal diffusivity [m^2·s^{-1}], which is calculated according to the Eq. (13):

$$a = \frac{k}{\rho\cdot c} \tag{13}$$

Eq. (12) is a second order differential equation that must be integrated in order to solve it and determine the thermal field. During the integration process, two integration constants appear and they must be fixed by means of initial and boundary conditions.

2.3. Initial and boundary conditions

The initial condition is referred to the temporal variable. In the present case, the workpiece is supposed to be at room temperature (25 °C) at the beginning of the process. On the contrary, boundary conditions (BC) are referred to the geometrical variables, where two BC can be distinguished: On the one hand, Dirichlet type BC is stablished in all the faces where the laser does not impact. In these faces, the elements next to them, but not belonging to the modeled volume, are considered to have the same temperature, and consequently, this is the same as imposing a Neumann BC where the heat flux is zero. On the other hand, Neumann BC is stablished in the element faces where the laser beam is focused.

The conductivity of the air is much smaller than that of the AISI 304 substrate, consequently, heat conductivity inside the air is neglected. Moreover, heat losses due to convection and radiation are considered in the faces of the elements that are in contact with the air. Convection and radiation coefficients are considered temperature independent, what avoids nonlinear effects [31], and they are modeled as heat sink sources when the thermal field equation, Eq. (12), is solved. On the one hand, Heigel et al. [32] studied the convection coefficient value in forced convection situations, for both vertical walls and horizontal surfaces. Based on the results, and the geometry being modeled, a constant convection coefficient of 20 W m^{-2} K^{-1} is defined. On the other hand, radiation losses are defined by the Stefan-Boltzmann law and emissivity is considered temperature independent, which is an assumption also adopted by Heigel et al. [32]. In Eq. (14), "n" represents the number of faces in contact with the atmosphere of each cell, where "h" and "ε" are the convection and emissivity coefficients, respectively, "T_∞" is the room temperature and "σ_b" is the Stefan-Boltzmann coefficient.

$$q_{losses} = [h\cdot(T - T_\infty) + \varepsilon\cdot\sigma_b\cdot(T^4 - T_\infty^4)]\cdot n \tag{14}$$

The laser beam is treated as a heat source that introduces a determined amount of energy into the modeled geometry. The laser beam is considered to have a Gaussian energy distribution where "r_l" is the beam radius at the surface of the substrate. Therefore, the energy density that the laser beam introduces in a determined point at the surface of the substrate can be calculated by means of the Eq. (15). In this equation, "α" is the material absorptivity and "x" and "y" define the planar distance between that point and the center of the laser beam. Besides, as stated Zhou et al. [33], the laser beam absorption is highly affected by the angle between the laser beam and the surface of the substrate, "δ", and therefore, this parameter is included in equation Eq. (15).

$$q_{laser} = \frac{2\cdot\alpha\cdot\cos(\delta)\cdot P_{real}}{\pi\cdot r_l^2}\cdot e^{-2\cdot\left(\frac{x^2+y^2}{r_l^2}\right)} \tag{15}$$

2.4. Central finite differences based solver

The resolution of the differential equations analytically is a complex task to achieve and even impossible in many cases. A conventional and

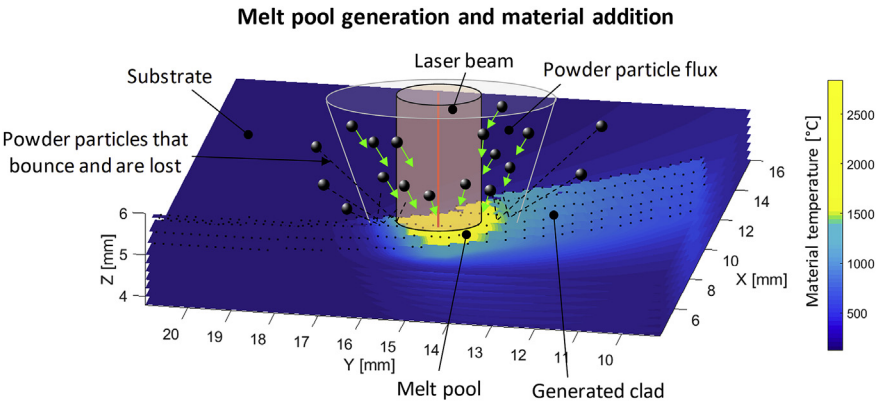

Fig. 1. Scheme of the material addition.

easy way to solve them is by discretizing the problem and transforming the differential equations into finite difference equations. A finite difference is based on the calculation of the mean variation of a variable in each time step. If the time step is short enough, then the finite difference tends to the derivative. Besides, a central finite difference scheme is used, because it introduces a smaller error than the incremental finite difference scheme. Furthermore, the fact that the equation has only second derivatives regarding the time reduces the size of the final equation and, therefore, the computational cost required for its resolution is also reduced. In the present model, an explicit formulation is used and, consequently, the equilibrium is set at the beginning of each time step.

$$\frac{\partial^2 T^t_{x,y,z}}{\partial y^2} \approx \frac{T^t_{x,y+\mathrm{d}y,z} - 2\cdot T^t_{x,y,z} + T^t_{x,y-\mathrm{d}y,z}}{\Delta y^2} \tag{17}$$

$$\frac{\partial^2 T^t_{x,y,z}}{\partial z^2} \approx \frac{T^t_{x,y,z+\mathrm{d}z} - 2\cdot T^t_{x,y,z} + T^t_{x,y,z-\mathrm{d}z}}{\Delta z^2} \tag{18}$$

$$\frac{\partial T^t_{x,y,z}}{\partial t} \approx \frac{T^{t+\mathrm{d}t}_{x,y,z} - T^t_{x,y,z}}{\Delta t} \tag{19}$$

After applying the central finite differences to Eq. (12), Eq. (20) is obtained and rearranging it in a matrix form, the following equation Eq. (21) is reached, where "$[M]$" is the transference matrix and "$\{F\}$" is the source vector. By means of this equation, the temperature field of the instant of time "$t + dt$" can be calculated based on the temperature field of the previous time interval "t". The criterion for ensuring the convergence is defined in Eq. (22).

$$\begin{aligned} T^{t+\mathrm{d}t}_{x,y,z} = T^t_{x,y,z} &+ a\cdot\frac{\Delta t}{\Delta x^2}\cdot(T^t_{x+\mathrm{d}x,y,z} - 2T^t_{x,y,z} + T^t_{x-\mathrm{d}x,y,z}) \\ &+ a\cdot\frac{\Delta t}{\Delta y^2}\cdot(T^t_{x,y+\mathrm{d}y,z} - 2T^t_{x,y,z} + T^t_{x,y-\mathrm{d}y,z}) \\ &+ a\cdot\frac{\Delta t}{\Delta z^2}\cdot(T^t_{x,y,z+\mathrm{d}z} - 2T^t_{x,y,z} + T^t_{x,y,z-\mathrm{d}z}) \pm \frac{q}{\rho.c}\cdot\Delta t \end{aligned} \tag{20}$$

$$\{T^{t+\mathrm{d}t}\} = [M]\cdot\{T^t\} + \{F\} \tag{21}$$

2.5. Convergence criteria

The von Neumann stability analysis is used for ensuring the convergence of the numerical model. Consequently, the maximum time step that ensures the convergence of the simulation is determined by the following equation:

$$\Delta t_{máx} = \left[2\cdot a\cdot\left(\frac{1}{\Delta x^2} + \frac{1}{\Delta y^2} + \frac{1}{\Delta z^2}\right)\right]^{-1} \tag{22}$$

Due to the dependence between the thermal diffusivity "a" and the temperature of the material, there is no fixed maximum time step that ensures the convergence. However, for the temperature range measured in the LMD process, the value of the maximum time step is limited to 10^{-3} s.

2.6. Material addition

Material addition is modeled as a two-step process for every time interval "Δt". In a first step, the thermal field of the substrate is calculated by means of Eq. (21). Afterwards, in a second step, the powder stream that interacts with the substrate is modeled and filler material is added in those elements that have exceeded the melting temperature.

In previous works carried by the authors, the powder distribution at the EHU-Coax2015 nozzle exit was modeled using the CFD software Fluent [34]. Besides, obtained results have been validated by means of an own developed mechanical measuring system based on a set of containers with different entrance holes [35]. At the working distance of the nozzle, which is situated at a 15 mm distance from the nozzle tip, the powder flux has a Gaussian distribution, with a maximum at the OZ rotation axis and a "r_p" radius. Consequently, the filled volume fraction of an element during the time step "Δt" can be calculated by means of Eq. (23), where "x" and "y" define the planar distance between that element and the center of the laser beam. Note that the material addition is proportional to the powder mass flow "$\dot{m}$".

$$\%_{fill} = \frac{2\cdot\dot{m}\cdot\Delta t}{\rho\cdot\Delta z\cdot\pi\Delta r_p^2}\cdot e^{-2\cdot\left(\frac{x^2+y^2}{r_p^2}\right)} \tag{23}$$

When the filled fraction of an element reaches the unit, this means that the element is filled with material. Hereafter, the model considers this element as substrate and automatically starts filling the upper element. Moreover, the heat transfer equation, Eq (21), is only solved in those elements completely filled with material, and therefore, the deposited bead only conducts through the substrate.

The assumption that all powder particles that fall inside the melt pool are added to the substrate is considered [14]. On the contrary, all particles that fall outside the melt pool bounce on the solid surface and are lost [11]. Hence, Eq. (23) is only activated in those elements whose the temperature is above the melting point. In Fig. 1, the material addition process is detailed, where the melt pool generated by the laser beam is represented.

3. Materials and methods

Experimental tests are carried out to validate the numerical model. Fig. 2 shows the manufactured test part, where an eight lap spiral is deposited using a 5-axis LMD machine Kondia Aktinos 500 (machine built by retrofitting a Kondia B500 conventional milling center and adding a 2-axis tilting table) coupled with a 1 kW Rofin Fiber laser. As it is shown in Fig. 2 (left) the EHU-Coax2015 nozzle is used in the

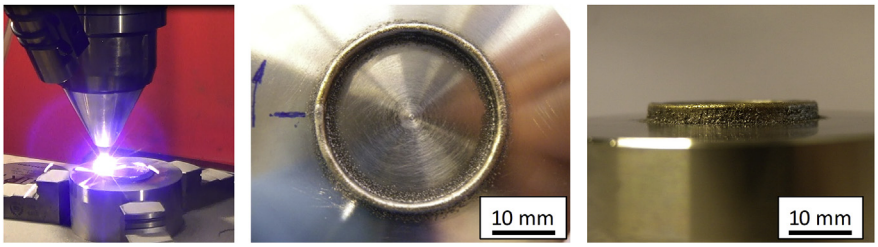

Fig. 2. Spiral test. Photo of the deposition process (left) and final shape of the generated geometry (center and right).

Table 1
Process parameters for the spiral test.

Parameter	Value
Laser Power [W]	625
Machine feed rate [mm·min^{-1}]	550
Laser beam radius [mm]	0.75
Powder spot radius [mm]	1.75
Powder flow rate [g·min^{-1}]	6

experimental tests. The resulting geometry is a cylinder of approximately 30 mm diameter and 3 mm height.

The test is used for analyzing the evolution of the thermal field as the height of the deposited geometry increases. Moreover, this test can be also used to evaluate the capability of the model to simulate the LMD process when clads are overlapped vertically. Table 1 presents the process parameter values used in the test. A Sulzer Metco Twin 10C powder feeder is employed for the powder injection and Argon is used as protective and drag gas. Both laser beam and powder stream at the working plane have a Gaussian distribution, whose radius are calculated as the radius corresponding to the circular area that encloses the e^{-2} (13.54%) of the maximum value.

Regarding the tested materials, both base and filler materials are AISI 304 stainless steel. The filler material has a particle size between 45 and 125 μm and was obtained by gas atomization, what ensures its sphericity. The AISI 304 is selected due to its relatively good aptitude for the LMD process and wide applications in the industry. Table 2 and Table 3 present the chemical composition and the thermal properties of the AISI 304, respectively.

Conductivity and specific heat values depend on the temperature of the material and in order to avoid abrupt variations of these properties, their values are defined as linear functions, what according to Gardner et al. is a good approximation to the real properties variation for austenitic stainless steels [36]. The linear functions are defined by their values at 20 °C and 1454 °C (liquidus temperature), which are obtained from Refs. [37] and [38] respectively.

The latent heat of fusion "*L*" is absorbed during the melting and released during solidification. Therefore, this energy input or output is included within the source vector defined in Eq. (21). Authors assume that the latent heat of fusion is uniformly distributed between the solidus and liquidus temperatures.

The attenuation of the laser beam produced by the powder particles during the inflight time is calculated based on a shadow model developed by Tabernero et al. [39] and resulted to be of 20.1%. Therefore, the value of the global losses coefficient "A" is set to 0.201, see Eq. (1). Besides, due to the interaction between the laser beam and the powder particles, the latter are heated. For the process parameters detailed in Table 1, powder particles have a 417.5 °C average temperature when they reach the melt pool surface. This value is measured experimentally using a thermographic camera (which has been previously calibrated by means of a two-color pyrometer).

Besides, a two-color pyrometer from IMPAC, with a measuring range between 550 and 2500 °C is used for measuring the temperature during the LMD process. The pyrometer is focused on the top of the substrate and follows the laser beam, but at an 8° angular displacement with regard to its center (see Fig. 3). The reason for not mounting a coaxial pyrometer and measuring directly in the center of the melt pool is to obtain a cleaner signal and avoid disturbances due to the interferences produced by the crossing powder particles. In Fig. 3, a schematic drawing of the experimental setup is detailed. The workpiece is situated at a 15 mm distance from the nozzle tip.

Table 2
AISI 304 chemical composition.

Component	C	Cr	Fe	Mn	Ni	P	S	Si
Wt [%]	≤0.08	18–20	balance	≤2	8–10.5	≤0.045	≤0.03	≤1

Table 3
AISI 304 properties [38].

Property	Symbol	Value
Density [kg·m^{-3}]	ρ	7200
Specific energy [J·kg^{-1}·K^{-1}]	c	500 + 0.181·(T-293)
Solidus temperature [K]	$T_{solidus}$	1697
Liquidus temperature [K]	$T_{liquidus}$	1727
Latent heat of fusion: [J·kg^{-1}]	L	$6.0 \cdot 10^4$
Conductivity [W·m^{-1}·K^{-1}]	k	16.2 + 0.013·(T-293)
Material absorptivity[a] [−]	α	0.3
Material emissivity [−]	ε	0.3

[a] Absorptivity value is determined based on previous works, where static single-laser-pulses were used for determining its value [18].

4. Numerical simulation of the microstructure, hardness and porosity formation

Once the geometry and thermal field are calculated, the model predicts the developed microstructure in each region and the reached hardness. Besides, it highlights the zones with the highest probability for pore formation.

The complete substrate is too large to be fully simulated and therefore, a 40 × 40 × 10 mm parallelepiped rectangle has been

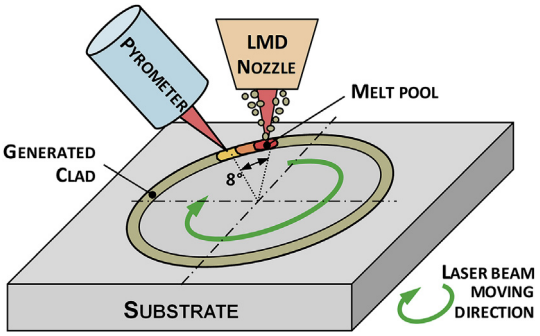

Fig. 3. Scheme of the setup used for measuring the temperature during the deposition of the spiral shaped geometry.

considered. A constant 0.20 mm element size has been stablished in order to achieve a relative high resolution with a reasonable computational cost. Moreover, in order to guarantee the stability of the forward Euler method, a 10^{-3} s time step has been stablished. Selected element size and time increase comply with the minimum requirements stablished by Zhang et al. in order to achieve an accurate solution [40]. On the one hand, Zhang et al. stablished that the time required for the laser beam to cover the distance corresponding to its radius (0.082 s in the present case) must be at least four times the time increment. On the other hand, they concluded that at least two elements are required per laser beam radius (0.75 mm). Therefore, both requirements are fulfilled.

4.1. Microstructure of the deposited material

As a result of the high cooling rates, the microstructure of the deposited material tends to present a dendritic structure [19]. The dendrite morphology depends mainly on the cooling rate and the developed thermal gradients inside the workpiece during the cooling process [41]. A lower cooling rate results in coarser Dendrite Arm Spacing (DAS) and a faster cooling rate in smaller DAS [42]. Therefore, based on the evolution of the temperature of each element in the simulated geometry, the model is capable of predicting the generated microstructure.

The primary DAS and the cooling rate are related by means of Eq. (24), where the coefficients "k" and "n" take the values of k = 80 and n = -0.33 for austenitic stainless steels [43]. The cooling rate is calculated during the solidification process. Therefore, "t_{l-s}" states the amount of time in which an element is between the liquidus and solidus temperatures and this temperature difference is represented by "ΔT".

$$DAS = k \cdot \left(\frac{\Delta T}{t_{l-s}}\right)^{n} \tag{24}$$

4.2. Hardness prediction

The final mechanical properties are driven mainly by the thermal history at each point and the consecutive heating and cooling cycles of the filler material and substrate during the LMD process. Thus, as a result of the microstructure variations, different hardness values are expected. Hardness variation due to the grainsize variation is well defined by the Hall-Petch equation. The coefficients of Eq. (25) depend on the material, and in the case of the AISI 304, Schino et al. [44] defined their values as H_0 = 135.1 [HV] and c = 174.5 [HV·μm$^{0.5}$].

$$H_{HP} = H_0 + c \cdot D^{-0.5} \tag{25}$$

However, other specific factors do influence the hardness of the deposited material. For example, Bhadeshia and Honeycombe concluded in their work that in the particular case of the AISI 304 a sensitization process occurs when the temperature of the material is risen around 660 °C [45]. This sensitization process is detrimental for the corrosion resistance of the material, because it precipitates chromium carbides in the grain boundaries. However, this same carbide precipitation also increases the hardness of the material.

The influence of the sensitization is considered by means of a hardening time variable "t_H", which defines the amount of time that a certain element is situated at a temperature range between 500 and 800 °C. Yan et al. stated in their work that chromium carbides are mainly generated in this temperature range [46]. Consequently, the hardness value due to the sensitization "H_S" is considered to be proportional to the "t_H" variable, Eq. (26), where "C" is the proportionality constant that must be calculated experimentally. In the case of the AISI 304 the value of this coefficient is set experimentally to a value of 8 [HV·s^{-1}].

$$H_S = C \cdot t_H \tag{26}$$

In order to determine the resulting hardness of the deposited material "H_{MODEL}", the Hall-Petch effect and the influence of the sensitization must be considered, Eq. (27).

$$H_{MODEL} = H_{HP} + H_S = (135.1 + 174.5 \cdot D^{-0.5}) + 8 \cdot t_H \tag{27}$$

4.3. Porosity formation modeling

Porosity formation is one of the typical defects of the LMD manufactured parts. Pores ranging between 10 and 100 microns can be found inside the deposited material and their formation is detrimental to the mechanical properties of the final part. Porosity generation is mainly driven by two factors: the gas trapped during the clad solidification [27] and the shrinkage of the material during the cooling stage [33]. Besides, the model considers the lack of fusion, which is due to an insufficient melting of the substrate [27], but it is not treated as porosity. Therefore, if the laser beam does not melt properly the base material, filler material does not adhere over the substrate and no clad is generated.

On the one hand, powder particles may drag gas inside the melt pool as they penetrate the molten surface. Thus, if the velocity of the solidifying front of the melt pool is higher than the exit velocity of the dragged gas, gas bubbles can get trapped inside the deposited material forming pores [47]. This is consistent with the conclusions reached by Zhou et al., who stated that porosity is reduced as the convection time of the melt pool is increased [33]. With the aim of predicting the region with the highest probability where trapped gas can appear, the model calculates the amount of time each element is in a liquid state. Afterwards, only those regions where this time is higher than a threshold value are highlighted, because of the higher probability of trapping gas.

On the other hand, shrink cavities can be generated when a liquid region of the deposited material is surrounded by solidified material. Due to the contraction of the material in the liquid-solid state change, voids may generate [33]. With the aim of evaluating this effect, a vector that indicates the relative cooling time between a certain node and the surrounding nodes is defined. For each node the relative solidification time "Δt^s" is calculated according to Eq. (28-33):

$$\Delta t^s_{x-\mathrm{dx},y,z} = t^s_{x-\mathrm{dx},y,z} - t^s_{x,y,z} \tag{28}$$

$$\Delta t^s_{x+\mathrm{dx},y,z} = t^s_{x+\mathrm{dx},y,z} - t^s_{x,y,z} \tag{29}$$

$$\Delta t^s_{x,y-\mathrm{dy},z} = t^s_{x,y-\mathrm{dy},z} - t^s_{x,y,z} \tag{30}$$

$$\Delta^s_{x,y+\mathrm{dy},z} = t^s_{x,y+\mathrm{dy},z} - t^s_{x,y,z} \tag{31}$$

$$\Delta t^s_{x,y,z-\mathrm{dz}} = t^s_{x,y,z-\mathrm{dz}} - t^s_{x,y,z} \tag{32}$$

$$\Delta t^s_{x,y,z+\mathrm{dz}} = t^s_{x,y,z+\mathrm{dz}} - t^s_{x,y,z} \tag{33}$$

When there is a void element in the mesh, the contribution of this node to the solidification front is zero, and therefore, its influence should be omitted. In order to introduce this boundary condition, the relative solidification time between a determined element and a void-adjacent element is imposed to be zero.

Combining Eq. (28-33), the time variable that indicates whether an element solidifies before or after the surrounding elements is calculated, see Eq. (34). A positive value indicates that the element solidifies after the surrounding elements, and therefore, shrinkage phenomena may happen. On the contrary, a negative value indicates that there is no risk of shrinkage.

$$\Delta t^s_{x,y,z} = \Delta t^s_{x-\mathrm{dx},y,z} + \Delta t^s_{x+\mathrm{dx},y,z} + \Delta t^s_{x,y-\mathrm{dy},z} + \Delta t^s_{x,y+\mathrm{dy},z} + \Delta t^s_{x,y,z-\mathrm{dz}} + \Delta t^s_{x,y,z+\mathrm{dz}} \tag{34}$$

In order to obtain a comparable time constant for each element, the time variable of an element calculated by means of Eq. (35) needs to be divided by the number of filled elements that are surrounding it (N).

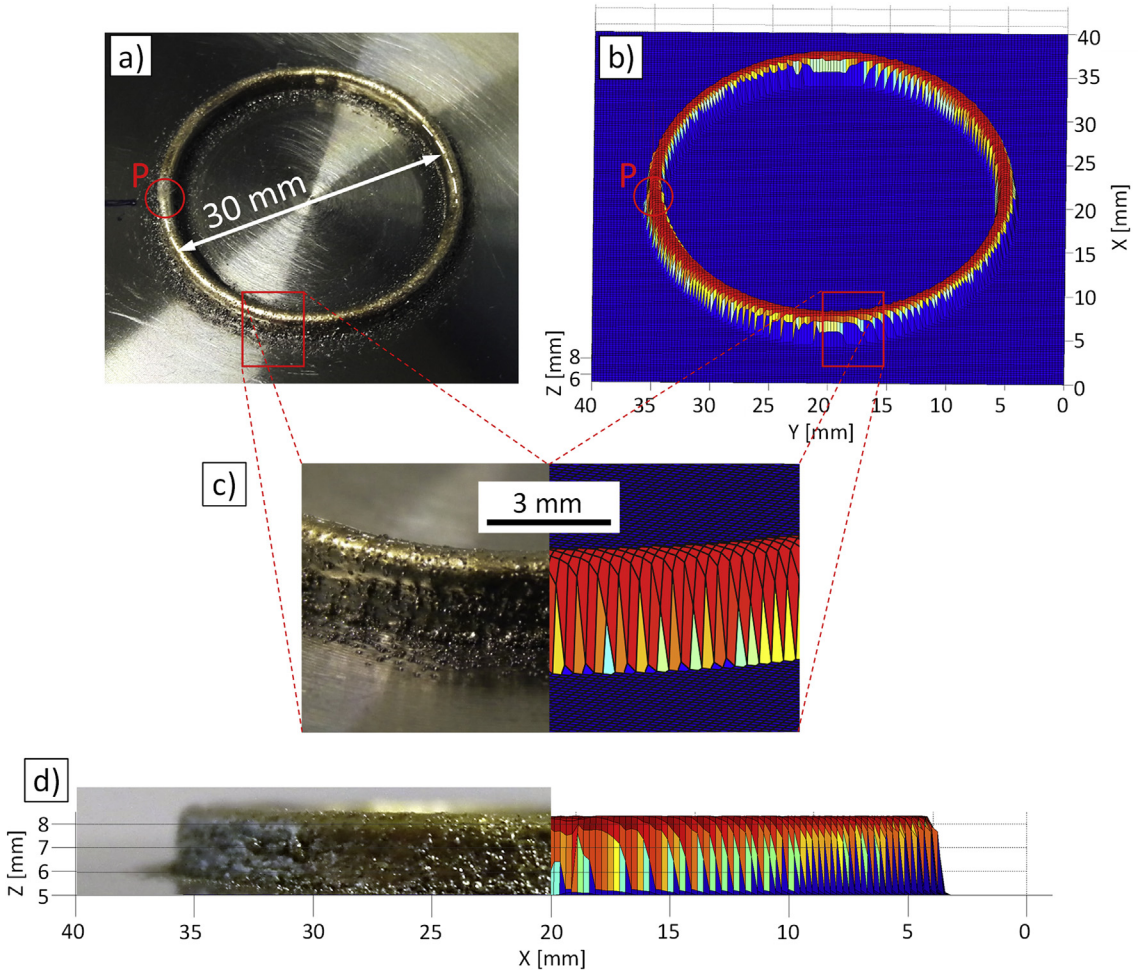

Fig. 4. Comparison between the geometry of the modeled and real part for the spiral test.

The parameter SCP states for the "Shrinking Cavity Probability".

$$SCP = \frac{\Delta t^{s}_{x,y,z}}{N} \tag{35}$$

5. Results and discussion

5.1. Geometry of the deposited clad

First, in order to validate the model, the estimated geometry of the spiral test is compared with that obtained experimentally. In Fig. 4 a 3D view of the simulated spiral next to a picture of the real spiral is shown. As it can be seen, the simulated geometry has a great resemblance to the real one.

The generated geometry has a flat surface. However, at the point where the clad deposition process starts and finishes (marked with the letter P and a red circle in Fig. 4), a small material accumulation is detected, what is in line with the experimental results. Besides, with the aim of obtaining a numerical value of the accuracy of the model, cross sections of the deposited spiral are compared with the model. In Fig. 5, the height profile of the modeled geometry (plotted in red) is represented over a real cross section of the spiral.

In both cases, four different cross sections are analyzed (sections situated at a 90° angular distance) and the height and width average values are calculated. Results obtained are compared in Table 4. As it can be seen, the numerical model is capable of predicting the geometry of the deposited clad with an error below 6%.

In the following figure, the estimated and experimental cross

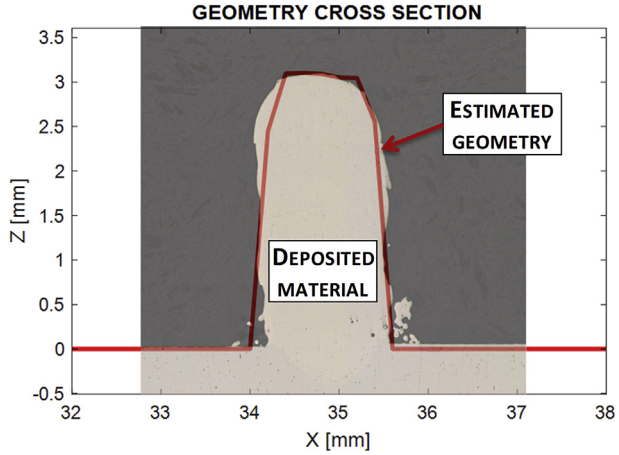

Fig. 5. Comparison between the cross sections of the deposited spiral for the modeled (red line) and real part. (For interpretation of the references to color in this figure legend, the reader is referred to the Web version of this article.)

Table 4
Comparison between the real and modeled dimensions of the deposited clad in the spiral tests.

Dimension	Real [mm]	Simulation [mm]	Error [%]
Clad height	3.109	3.103	−0.193
Clad width	1.483	1.400	−5.597

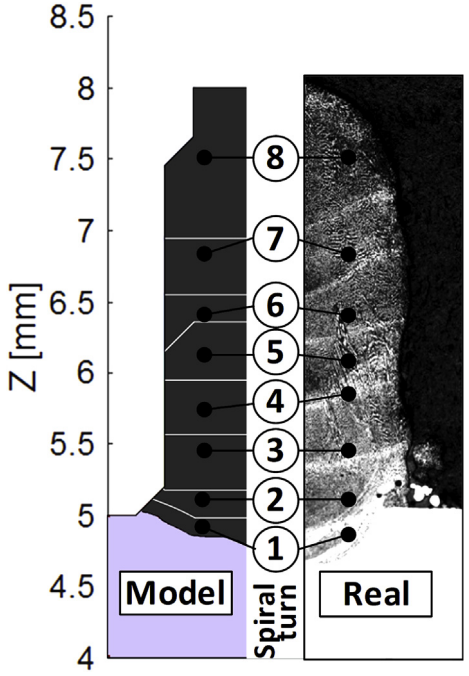

Fig. 6. Comparison between the modeled and the experimentally deposited layers.

sections of the spiral are shown. The deposited layers with each turn of the spiral are highlighted. In the experimental case, the cross section is etched electrolytically using oxalic acid in order to stand out the different layers. It can be concluded that a reasonable agreement is obtained (see Fig. 6).

5.2. Evolution of the temperature field

Hereafter, a comparison between the real and modeled temperature fields is presented. With the aim of validating the capability of the model to simulate the thermal field, in Fig. 7 (right) the evolution of the temperature measured by the pyrometer (blue line) and the temperature predicted by the model (red line) are compared. As it is shown, the measured temperature goes on increase as the interaction time between the laser beam and the workpiece increases. This is because the temperature of the base material also increases. Moreover, the greater the height of the deposited spiral, the lower is the dissipation of the heat introduced by the laser. In Fig. 7 (left) the modeled thermal field during the deposition of the eighth lap of the spiral is shown. It is concluded that the model simulates the thermal field with an acceptable accuracy.

5.3. Cooling rate and microstructure

The solidifying time is defined as the time period in which the temperature of a certain element is between the solidus and the liquidus temperatures. As it can be seen in Fig. 8, a higher solidifying time is obtained in the upper part of the generated spiral, what is consistent with the experimental measurements, since the heat dissipation is lower. On the basis of the solidifying time, the cooling rate is obtained, which is inversely proportional to the solidifying time. In order to avoid numerical instabilities, instead of using directly the modeled value of the cooling rate, a 4th order polynomic approximation is used for the calculation of the DAS value (see Fig. 8).

In Fig. 9, the experimentally measured and the estimated DAS value obtained from the model are compared. As it is shown, samples are taken in the centerline of the built wall. Good agreement is obtained, with an error below 1 micron. Therefore, it can be concluded that the DAS value depends mainly on the cooling rate and the model is capable of predicting the microstructure of the deposited material.

Besides, in Fig. 9, details of the microstructure in various regions situated at different distances from the surface of the substrate are shown. Basically, two zones are distinguished: The light regions represent the γ-austenite phase, whereas the dark regions represent the δ-ferrite phase. In the upper part of the spiral, where the cooling rate is lower, coarser dendrites are obtained and even secondary dendrites can be distinguished. In the lower part of the spiral, the generated dendrites are much thinner, and no secondary arms of the dendrites are found.

5.4. Hardness variation inside the deposited material

In Fig. 10 (left) the amount of time during which each node is at a temperature range between 500 and 800 °C is represented. The variation of this time variable in the centerline of the built wall is represented in Fig. 10 (right) with a blue line. The same figure also shows the real hardness profile in the centerline of the cross section, represented with a red line. To this end, a cross section of the deposited spiral is extracted, grinded and polished. Afterwards, the microhardness value is measured using a Knoop indenter, together with a 300 g load and a 12 s dwell time. In order to obtain a representative profile that describes the variation of the hardness, an indentation is made every 0.25 mm.

If only the Hall-Petch relation is used for predicting the resulting hardness of the deposited material, see Table 5, the experimental hardness measurements differ from those predicted by the model. However, if this value is corrected by the hardness increase due to the sensitization, an error below 10% is obtained.

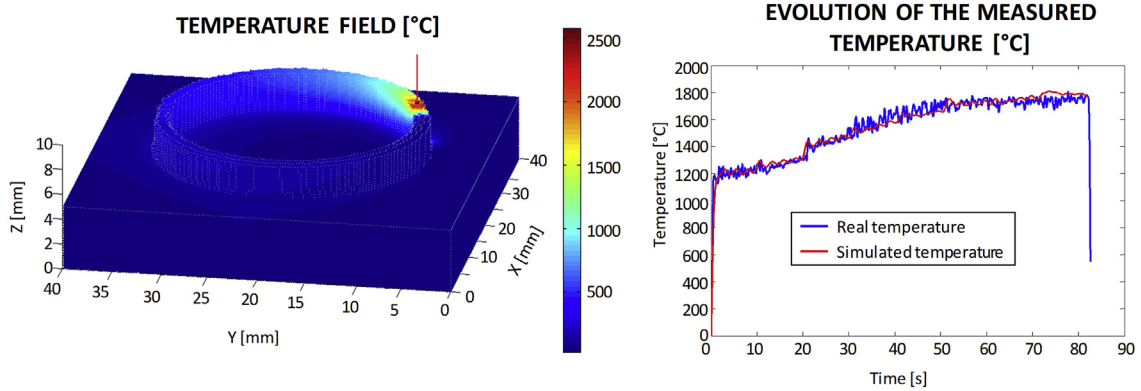

Fig. 7. The modeled thermal field during the deposition of the eighth lap (left) and a comparison between the real and simulated temperatures during the deposition of the whole spiral (right).

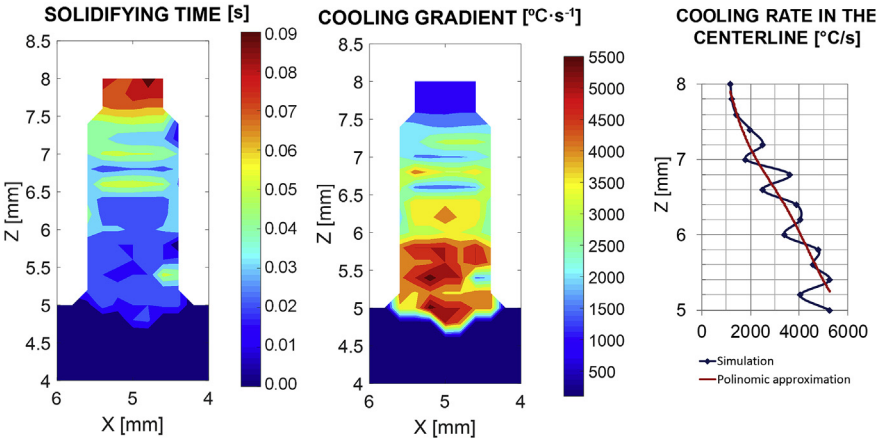

Fig. 8. Cross section of the modeled spiral where the elements are colored according to the solidification time (left) and the cooling rate (center). Variation of the cooling rate in the centerline is shown on the right.

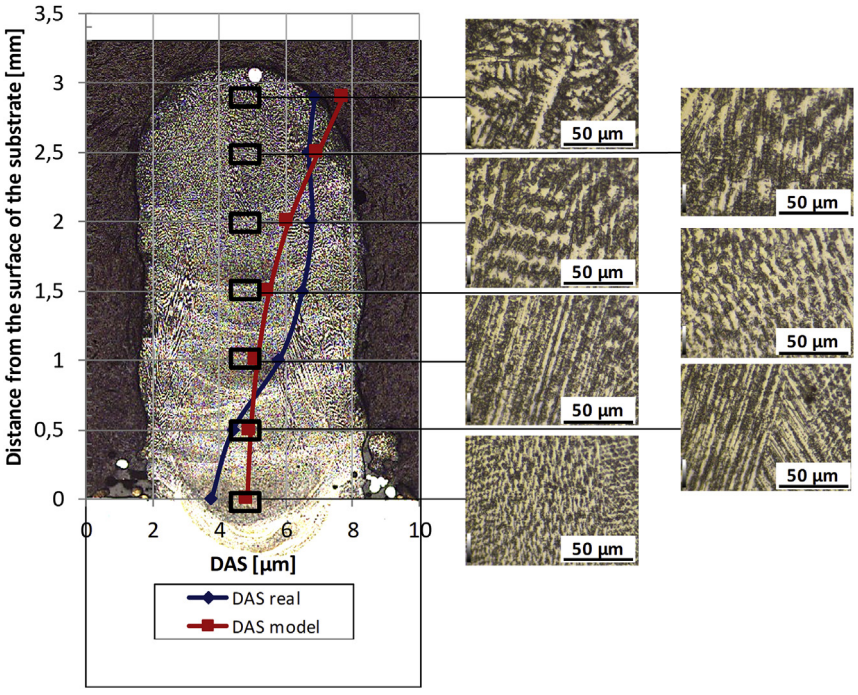

Fig. 9. Comparison between the real and the modeled DAS.

5.5. Porosity evaluation

The analysis of the porosity formation is a qualitative procedure. The two mechanisms detailed in section "*4.3. Porosity formation modeling*" for the pore generation are considered. The regions where the risk of pore formation is maximum are detected and highlighted by the model. Fig. 11 (left) shows the solidification time of the deposited material in each element. In Fig. 11 (center) the Shrinking Cavity Probability (SCP) values are displayed. Finally, in Fig. 11 (right) the experimental test results are shown, where the real porosity is analyzed in a cross section of the spiral.

Porosity is found in the lower part of the generated spiral; the area is named with the letter "A" in Fig. 11. Their origin could be both: a low molten time of the material, and therefore, an insufficient time for the trapped gas to exit the melt pool, or the fact that shrinking cavities are generated. Besides, pores are found in the upper part of the spiral, named with the letter "B" in Fig. 11. Their origin is clearly a low molten time. This statement is confirmed by the powder particle, trapped but not melted, found inside the spiral, named with the letter "C" in Fig. 11. Due to the fast solidification of the molten material, the powder particle is not melted, what justifies the statement that the pores next to it are due to a low molten time, note that this lack of fusion of the powder particle is not considered as porosity. Moreover, the regions where the model predicts that no pores should appear are analyzed and no porosity is found. In total, four cross sections are analyzed and in all of them, the same porosity pattern is detected.

6. Conclusions

In conclusion, a 3D numerical model has been developed for LMD and validated for the case of AISI 304. Accordingly, the main conclusions are drawn as it follows:

(1) Agreement is obtained between the modeled geometry of the clad and the experimentally measured results. An error below 6% is measured when comparing the model results and the average measurements, what justifies the accuracy of the model. However, the size of the part is a limiting factor and if the size of the modeled

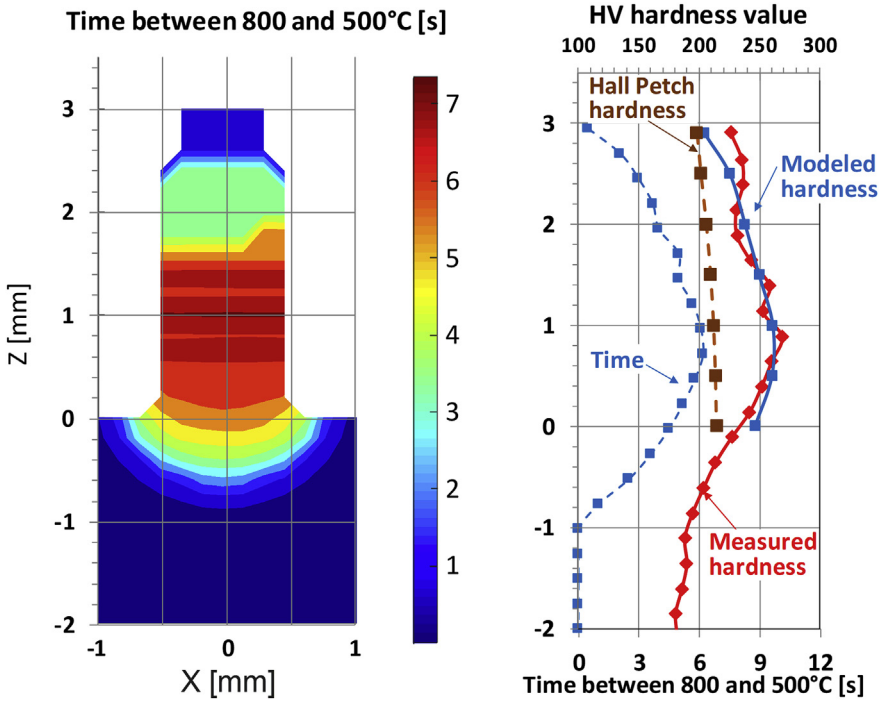

Fig. 10. Comparison between the real hardness measured in the centerline of the cross section and the amount of time in which each element is situated between 500 and the 800 °C.

Table 5
Hardness modeling.

Z [mm]	Modeled DAS [μm]	Hall Petch hardness, H_{HP} [HV]	t_H [s]	$H_{MODEL} = H_{HP} + C \cdot t_H$ [HV]	H_{REAL} [HV]	Error [%]
2.9	7.7	198.0	0.8	204.4	224.2	−8.8
2.5	6.9	201.3	3.0	225.3	236.4	−4.7
2.0	6.1	205.9	4.0	237.9	231.6	2.7
1.5	5.5	209.6	5.0	249.6	258.7	−3.5
1.0	5.1	212.1	6.1	260.9	268.9	−3.0
0.5	4.9	213.7	5.8	260.1	251.9	3.3
0	4.8	214.6	4.5	246.1	227.1	8.4

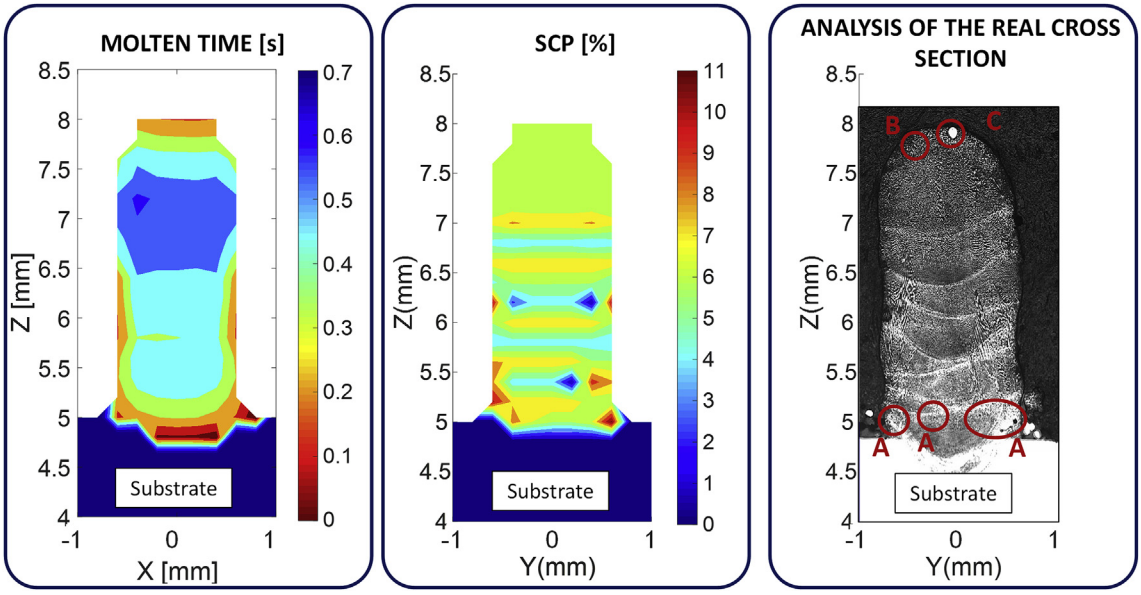

Fig. 11. Pore apparition prediction according to the molten time (left) and the Shrinking Cavity Probability (center) and the analysis of the real cross section (right) where the detected pores are highlighted.

geometry were higher than 100 × 100 × 100 mm, the computational cost would be extremely high. This is why, it is not possible to simulate the whole part and proper boundary conditions must be stablished.

(2) The reached temperatures during the LMD process are experimentally measured using a two-color pyrometer and compared with the values provided by the model. Good agreement is obtained. The model is capable of predicting the temperature increase of the substrate as the interaction time between the laser beam and the substrate increases. The determination of the thermal field is of major importance in the LMD process, because in addition to the geometry of the clad, it determines the resulting mechanical properties.

(3) The model is capable of determining the Dendrite Arm Spacing (DAS) of the deposited material based on the cooling rate of each element. An error below 1 micron is obtained between the values measured experimentally and the values obtained from the numerical simulation.

(4) Based on the thermal field and setting empirically the value of a proportional coefficient "*C*", the model is capable of predicting the resulting hardness of the deposited material, with an error below 10%. For this purpose, both Hall-Petch relation and sensitization are considered.

(5) The model is capable of predicting the pore generation on the basis of two mechanisms: the trapped gas during the deposition process and the shrinkage cavities generated due to the contraction of the material during the cooling process. Consequently, this tool can be used to predict the probability of porosity formation and optimize the deposition strategies in order to avoid their apparition.

The model can simulate the LMD process only in three translational axes (X, Y and Z) and no rotational movements have been included. In future works the model will be adapted to simulate the LMD process in 5-axis (3 translations and 2 rotations).

Acknowledgements

Authors gratefully acknowledge "LaCaixa" foundation for its financial help. In addition, this work has been founded by the H2020-FoF13-2016 PARADDISE project (contract No.: 723440). This work has been also carried out in the framework of the DPI2016-79889-R – INTEGRADDI project, funded by the Spanish Ministry of Industry and Competitiveness.

References

[1] D. Herzog, V. Seyda, E. Wycisk, et al., Additive manufacturing of metals, Acta Mater. 117 (2016) 371–392.
[2] E. Toyserkani, A. Khajepour, S. Corbin, Laser Cladding, CRC Press LLC, 2005.
[3] D. Appleyard, Powering up on power technology, Met. Powder Rep. 70 (2015) 285–289.
[4] J.M. Flynn, A. Shokrani, S.T. Newman, V. Dhokian, Hybrid additive and subtractive machine tools – research and industrial developments, Int. J. Mach. Tool Manufact. 101 (2016) 79–101.
[5] A. Peng, Y. Taiping, L. Sheng, L. Dongsheng, H. Qianwu, X. Weihao, Z. Xiaoyan, Direct laser fabrication of nickel alloy samples, Int. J. Mach. Tool Manufact. 45 (2005) 1288–1294.
[6] H. Shipley, D. McDonnell, M. Culleton, R. Coull, R. Lupoi, G. O'Donnell, D. Trimble, Optimisation of process parameters to address fundamental challenges during selective laser melting of Ti-6Al-4V: a review, Int. J. Mach. Tool Manufact. 128 (2018) 1–20.
[7] V. Ocelík, O. Nenadl, A. Palavra, JThM. De Hosson, On the geometry of coating layers formed by overlap, Surf. Coating. Technol. 242 (2014) 54–61.
[8] O. Nenadl, V. Ocelík, A. Palavra, JThMD. Hosson, The prediction of coating geometry from main processing parameters in laser cladding, Phys. Procedia 56 (2014) 220–227.
[9] W. Ya, B. Pathiraj, S. Liu, 2D modelling of clad geometry and resulting thermal cycles during laser cladding, J. Mater. Process. Technol. 230 (2016) 217–232.
[10] A.J. Pinkerton, Advances in the modeling of laser direct metal deposition, J. Laser Appl. 27 (2015) S15001.
[11] P. Peyre, P. Aubry, R. Fabbro, R. Neveu, A. Longuet, Analytical and numerical modelling of the direct metal deposition laser process, J. Phys. Appl. Phys. 41 (2008) 025403.
[12] A. Pinkerton, L. Li, The significance of deposition point standoff variations in multiple-layer coaxial laser cladding (coaxial cladding standoff effects), Int. J. Mach. Tool Manufact. 44 (2004) 573–584.
[13] L. Han, K.M. Phatak, F.W. Liu, Modeling of laser deposition and repair process, J. Laser Appl. 17 (2005) 89–99.
[14] A. Pinkerton, L. Lin, Modelling the geometry of a moving laser melt pool and deposition track via energy and mass balances, J. Phys. Appl. Phys. 37 (2004) 1885–1895.
[15] M. Alimardani, E. Toyserkani, J.P. Huisson, 3D numerical approach for geometrical prediction of multiplayer solid freeform fabrication process, J. Laser Appl. 19 (2007) 14–25.
[16] R. Vilar, E.C. Santos, P.N. Ferreira, et al., Structure of NiCrAlY coatings deposited on single-crystal alloy turbine blade material by laser cladding, Acta Mater. 57 (2009) 5292–5302.
[17] P. Promoppatum, S.C. Yao, P.C. Pistorius, A.D. Rollett, P.J. Coutts, F. Lia, R. Martukanitz, Numerical modeling and experimental validation of thermal history and microstructure for additive manufacturing of an Inconel 718 product, Prog. Addit. Manuf. (2018) 1–18 https://doi.org/10.1007/s40964-018-0039-1.
[18] J.I. Arrizubieta, A. Lamikiz, F. Klocke, S. Martínez, K. Arntz, E. Ukar, Evaluation of the relevance of melt pool dynamics in Laser Material Deposition process modeling, Int. J. Heat Mass Tran. 115 (2017) 80–91.
[19] V. Ocelík, I. Furár, JThM. De Hosson, Microstructure and properties of laser clad coatings studied by orientation imaging microscopy, Acta Mater. 58 (2010) 6763–6772.
[20] Z. Liu, H. Qi, L. Jiang, Control of crystal orientation and continuous growth through inclination of coaxial nozzle in laser powder deposition of single-crystal superalloy, J. Mater. Process. Technol. 230 (2016) 177–186.
[21] M. Valdez, C. Kozuch, E.J. Faierson, I. Jasiuk, Induced porosity in Super Alloy 718 through the laser additive manufacturing process: microstructure and mechanical properties, J. Alloy. Comp. 725 (2017) 757–764.
[22] A. Bandyopadhyay, F. Espana, V. Krishna Balla, S. Bose, Y. Ohgami, N.M. Davies, Influence of porosity on mechanical properties and in vivo response of Ti6Al4V implants, Acta Biomater. 6 (2010) 1640–1648.
[23] W.H. Zhang, H. Tsai, pore formation and prevention in deep penetration pulsed laser welding, ICALEO 2002 - 21st International Congress on Applications of Laser and Electro-optics, Congress Proceedings, Laser Institute of America, 2002, pp. 14–17.
[24] R. Li, Y. Shi, Z. Wang, L. Wang, J. Liu, W. Jian, Densification behavior of gas and water atomized 316L stainless steel powder during selective laser melting, Appl. Surf. Sci. 256 (2010) 4350–4356.
[25] M. Xia, D. Gu, G. Yu, D. Dai, H. Chen, Q. Shi, Porosity evolution and its thermodynamic mechanism of randomly packed powder-bed during selective laser melting of Inconel 718 alloy, Int. J. Mach. Tool Manufact. 116 (2017) 96–106.
[26] C. Zeng, W. Tian, W.H. Liao, et al., Microstructure and porosity evaluation in laser cladding deposited Ni-based coatings, Surf. Coating. Technol. 294 (2016) 122–130.
[27] B. Borges, L. Quintino, R.M. Miranda, P. Carr, Imperfections in laser clading with powder and wire fillers, Int. J. Adv. Manuf. Technol. 50 (2010) 175–183.
[28] F. Lia, J. Park, J. Tressler, R. Martukanitz, Partitioning of laser energy during directed energy deposition, Addit. Manuf. 18 (2017) 31–39.
[29] F. Wirth, S. Arpagaus, K. Wegener, Analysis of melt pool dynamics in laser cladding and direct metal deposition by automated high-speed camera image evaluation, Addit. Manuf. 21 (2018) 369–382.
[30] Y.P. Lei, H. Murakawa, Y.W. Shi, X.Y. Li, Numerical analysis of the competitive influence of Marangoni flow and evaporation on heat surface temperature and molten pool shape in laser surface remelting, Comput. Mater. Sci. 21 (2001) 276–290.
[31] M. Labudovic, D. Hu, R. Kovacevic, A three dimensional model for direct laser metal powder deposition and rapid prototyping, J. Mater. Sci. 38 (2003) 35–49.
[32] J.C. Heigel, P. Michaleris, E.W. Reutzel, Thermo-mechanical model development and validation of directed energydeposition additive manufacturing of Ti–6Al–4V, Addit. Manuf. 5 (2015) 9–19.
[33] C. Zhou, S. Zhao, Y. Wang, F. Liu, W. Gao, X. Lin, Mitigation of pores generation at overlapping zone during laser cladding, J. Mater. Process. Technol. 216 (2015) 369–374.
[34] J.I. Arrizubieta, I. Tabernero, J.E. Ruiz, A. Lamikiz, S. Martinez, E. Ukar, Continuous coaxial nozzle design for LMD based on numerical simulation, Phys. Procedia 56 (2014) 429–438.
[35] J.I. Arrizubieta, S. Martinez, A. Lamikiz, et al., Instantaneous powder flux regulation system for Laser Metal Deposition, J. Manuf. Process. 29 (2017) 242–251.
[36] L. Gardner, A. Insausti, K.T. Ng, M. Ashra, Elevated temperature material properties of stainless steel alloys, J. Constr. Steel Res. 66 (2010) 634–647.
[37] AISI 304 Datasheet, ASM Aerospace specification Metals Inc., Available: http://asm.matweb.com/search/SpecificMaterial.asp?bassnum=mq304a (Online, accessed 07.08.2018).
[38] S. Pang, X. Chen, W. Li, et al., Efficient multiple time scale method for modeling compressible vapor plume dynamics inside transient keyhole during fiber laser welding, Optic Laser. Technol. 77 (2016) 203–214.
[39] I. Tabernero, A. Lamikiz, S. Martínez, E. Ukar, L.N. López de Lacalle, Modelling of energy attenuation due to powder flow-laser beam interaction during laser cladding process, J. Mater. Process. Technol. 212 (2012) 516–522.
[40] L. Zhang, E.W. Reutzel, P. Michaleris, Finite element modeling discretization requirements for the laser forming process, Int. J. Mech. Sci. 46 (2004) 623–637.
[41] A. Shah, A. Kumar, J. Ramkumar, Analysis of transient thermo-fluidic behavior of melt pool during spot laser welding of 304 stainless-steel, J. Mater. Process.

Technol. 256 (2018) 109–120.
[42] W. Tan, N.S. Bailey, Y.C. Shin, Numerical modeling of transport phenomena and dendritic growth in laser conduction welding of 304 stainless steel, International Manufacturing Science and Engineering Conference, Vol. 1 ASME, 2011, pp. 243–251.
[43] J.W. Fu, Y.S. Yang, J.J. Guo, et al., Effect of cooling rate on solidification microstructures in AISI 304 stainless steel, Mater. Sci. Technol. 24 (2008) 941–944.
[44] A. Di Schino, M. Salvatori, J.M. Kenny, Effects of martensite formation and austenite reversion on grain refining of AISI 304 stainless steel, J. Mater. Sci. 7 (2002) 4561–4565.
[45] H. Bhadeshia, R. Honeycombe, Steels: Microstructure and Properties, third ed., Butterworth-Heinemann, 2006.
[46] J. Yan, M. Gao, X. Zeng, Study on microstructure and mechanical properties of 304 stainless steel joints by TIG, laser and laser-TIG hybrid welding, Optic Laser. Eng. 48 (2010) 512–517.
[47] D. Triantafyllidis, L. Li, F.H. Stott, Mechanisms of porosity formation along the solid/liquid interface during laser melting of ceramics, Appl. Surf. Sci. 208–209 (2003) 458–462.